communications biology

Article

https://doi.org/10.1038/s42003-025-07485-2

Structural basis for assembly and function of the *Salmonella* flagellar MS-ring with three different symmetries

Miki Kinoshita [1,2], Fumiaki Makino[1,2,3], Tomoko Miyata[1,2], Katsumi Imada [4], Keiichi Namba [1,2] ✉ & Tohru Minamino [1] ✉

The flagellar MS-ring is the initial template for flagellar assembly and houses the flagellar protein export complex. The MS-ring has three parts of different symmetries within the ring structure by assembly of FliF subunits in two different conformations with distinct arrangements of three ring-building motifs, RBM1, RBM2, and RBM3. However, it remains unknown how these symmetries are generated. A combination of cryoEM structure and structure-based mutational analyses demonstrates that the well-conserved DQxGxxL motif in the RBM2-RBM3 hinge loop allows RBM2 to take two different orientations relative to RBM3. Of 34 FliF subunits of the MS-ring in the basal body, 23 RBM2 domains form an inner ring with a central pore that accommodates the flagellar protein export complex, and the remaining 11 RBM2 domains form 11 cog-like structures together with RBM1 domains just outside the inner RBM2-ring. We propose that a dimer of FliF with two different conformations initiates MS-ring assembly.

The flagellum of *Salmonella enterica* serovar Typhimurium (hereafter referred to as *Salmonella*) is a supramolecular motility machine consisting of three parts: the basal body, which acts as a bi-directional rotary motor; the filament, which functions as a helical propeller; and the hook, which serves as a universal joint to smoothly transmit motor torque to the filament[1,2].

The *Salmonella* basal body consists of the MS-ring, the C-ring, the LP-ring, and the rod[3,4]. Although structural work has identified that MS-rings can form multiple symmetries[5–7], only MS-rings with C34 symmetry have been observed in the native basal body[8–10]. The MS-ring is formed entirely of FliF subunits[11,12], and FliG uses the MS-ring as a scaffold for its ring assembly[13]. The FliM-FliN complex assembles onto the FliG-ring through an interaction between FliG and FliM to form the C-ring[14,15]. Interestingly, the C-ring symmetry varies from 32-fold to 36-fold, with 34-fold being the most common[10,16–18]. Together, there is the possibility that MS-rings with different symmetries may be present in intact flagella. Other symmetries could also have a distinct biological function. This provides the rationale for investigating MS-rings without 34-fold symmetry, even though they have not been observed in intact basal bodies to date.

The MS-C-ring complex acts as the rotor of the flagellar motor. The MotA-MotB complex, which contains 5 MotA subunits and 2 MotB subunits, assembles around the rotor through an interaction between MotA and FliG. It acts as one of up to 11 stator units in the flagellar motor[19]. The C-ring serves as a reversible gear that allows the motor to rotate both counter-clockwise (CCW) and clockwise (CW)[20].

FlgH and FlgI form the LP-ring with C26 symmetry. The LP-ring functions as a bushing for high-speed rotation of the rod, which acts as the drive shaft of the flagellar motor[8,9,21]. The rod is a helical tubular structure with about 5.5 subunits per one helical turn[22]. It is divided into two parts: the proximal rod, which is composed of 6 FliE, 5 FlgB, 6 FlgC, and 5 FlgF subunits; and the distal rod composed of 24 FlgG subunits[8,9,23,24]. The proximal and distal rods are located inside the MS-ring and LP-ring, respectively. The basal body also contains the flagellar type III secretion system (hereafter referred to as fT3SS) that transports flagellar structural subunits from the cytoplasm to the distal end of the growing flagellum for construction of the extracellular flagellar structure[25]. The fT3SS comprises a transmembrane export-gate complex with a subunit stoichiometry of 9 FlhA, 1 FlhB, 5 FliP, 4 FliQ, and 1 FliR, and a cytoplasmic ATPase ring with a subunit stoichiometry of 12 FliH, 6 FliI, and 1 FliJ. The export-gate complex is housed in the central pore of the MS-ring, whereas the cytoplasmic ATPase complex attaches to the C-ring via struts made up of FliH dimers[26,27]. Thus, the MS-ring is the initial structure that determines flagellar assembly and function.

Salmonella FliF (UniProt ID: P15928) consists of 560 amino acid residues with two predicted transmembrane helices (residues 26–46 and

[1]Graduate School of Frontier Biosciences, Osaka University, Suita, Osaka, Japan. [2]JEOL YOKOGUSHI Research Alliance Laboratories, Osaka University, Suita, Osaka, Japan. [3]JEOL Ltd., Akishima, Tokyo, Japan. [4]Department of Macromolecular Science, Graduate School of Science, Osaka University, Toyonaka, Osaka, Japan. ✉e-mail: keiichi@fbs.osaka-u.ac.jp; tohru@fbs.osaka-u.ac.jp

residues 455–475). It forms the M-ring, the S-ring, and the β-collar[5]. The M-ring is embedded within the cytoplasmic membrane, whereas the S-ring and the β-collar are in the periplasmic space. The C-terminal cytoplasmic domain of FliF interacts with the N-terminal domain of FliG to connect the C-ring with the MS-ring[28].

A large periplasmic region (residues 47–454) between the two transmembrane helices contains three ring-building motifs: RBM1 (residues 60–124), RBM2 (residues 125–215), and RBM3 (residues 228–438). RBM3 is subdivided into three regions: RBM3a (residues 228–270), β-collar (residues 271–381), and RBM3b (residues 382–438). RBM3a and RBM3b form a single core domain (hereafter referred to as the S-ring domain) that assembles to form the S-ring. The β-collar domain consists of two sets of antiparallel β-sheets and forms a cylindrical β-barrel structure that extends above the S-ring. The β-collar structure tightly and stably accommodates the proximal rod[5].

RBM2 is placed in two distinct orientations relative to the S-ring. In the MS-ring of the native flagellar basal body, which consists of 34 FliF subunits, the RBM2 domains of 23 subunits are placed inside the M-ring to form its inner core ring (hereafter referred to as RBM2-ring), whereas the RBM2 domains of 11 subunits interact intramolecularly with RBM1 to generate 11 cog-like structures just outside the RBM2-ring. As a result, the export-gate complex of the fT3SS is firmly and stably accommodated within the central pore of the RBM2-ring. To achieve the C34, C23, and C11 rotational symmetries of the MS-ring, RBM2 must have very different orientations in different FliF subunits[5,10,29]. However, it is unclear how during MS-ring assembly different FliF subunits take on different conformations.

To address this question, we performed cryo-electron microscopy (cryoEM) structural analyses of the *Salmonella* MS-ring formed by FliF co-expressed with FliG and proteins of the transmembrane export-gate complex and obtained the structure of a 33-mer MS-ring at 3.1 Å resolution. We also performed mutational analyses of regions of FliF that the structural analysis indicated were important in determining the conformation of the MS-ring. In particular, a highly flexible region consisting of residues 163–168 in RBM2 is required for efficient assembly of the export gate into the MS-ring. We also tested the importance of the conformational flexibility of a hinge loop (residues 214–228) connecting RBM2 and RBM3 in allowing two different orientations of RBM2 relative to RBM3. One of these conformations allows 22 RBM2 domains to form the 22-mer RBM2-ring. The other allows 11 RBM2 domains to interact intramolecularly with RBM1 to form 11 discrete cog-like structures at the periphery of the RBM2-ring. We also investigated the importance of the well-conserved Ile-252 residue in maintaining hydrophobic contacts that are necessary for the integrity of the S-ring. Based on the structural and mutational studies, we propose a mechanism of MS-ring formation with three different rotational symmetries.

Results

CryoEM structural analysis of the MS-ring

The MS-ring is not only the structural template for FliG-ring formation but also the housing for the transmembrane export-gate complex made up of FlhA, FlhB, FliP, FliQ, and FliR (Fig. 1). FliO is required for efficient formation of the $FliP_5$-$FliQ_4$-$FliR_1$ complex before the export-gate complex incorporates into the central pore of the M-ring during MS-ring formation[30,31]. Therefore, in this study, FliF was co-expressed with FlhA, FlhB, FliG, FliO, FliP, FliQ, and FliR from a pTrc99-based plasmid in *Salmonella* SJW1368 cells, in which the flagellar master operon *flhDC*, which is required for the expression of all flagellar genes is deleted. Fractions containing FliF, FliG, and FlhA were separated from solubilized crude membranes using sucrose gradient ultracentrifugation (Supplementary Fig. 1a). Ring-shaped particles were observed in both negatively stained EM images (Supplementary Fig. 1b) and cryoEM images (Supplementary Fig. 2a). In the flagellar basal body, FlhA is located inside the MS-ring along with other export-gate proteins[30,32,33], and its C-terminal cytoplasmic domain forms a homo-nonameric ring structure that projects into the central cavity of the C-ring[34,35]. Although FliG and FlhA were associated with the purified MS-ring (Supplementary Fig. 1a), the FliG-ring and the export-gate complex were not visible in our cryoEM images.

A total of 1,015,741 particles were extracted from 4,885 micrographs and analyzed. It has been shown that the MS-ring formed by co-expression of full-length FliF with FliG, FliM, and FliN has rotational symmetry ranging from 32-fold to 34-fold. The 33-mer rings are the most common (about 80% of the population), followed by the 34-mer rings (about 15% of the population) and the 32-mer rings (about 5% of the population)[6]. In the present cryoEM analysis, representative 3D classification revealed that

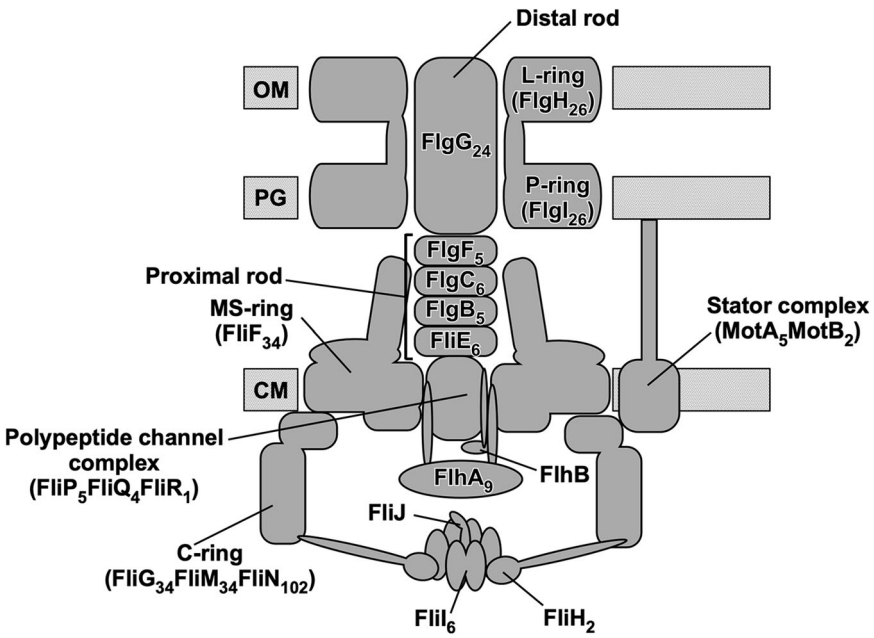

Fig. 1 | Schematic diagram of the flagellar basal body. The flagellar basal body consists of the C-ring (FliG, FliM, FliN), MS-ring (FliF), P-ring (FlgI), L-ring (FlgH), and rod (FliE, FlgB, FlgC, FlgF, FlgG). Multiple stator units, each of which is formed by 5 MotA subunits and 2 MotB subunits, surround the basal body. The basal body also contains a type III secretion system consisting of a transmembrane export gate complex (FlhA, FlhB, FliP, FliQ, FliR) and a cytoplasmic ATPase ring complex (FliH, FliI, FliJ). The MS-C-ring complex acts as a rotor of the flagellar motor. The P and L rings together form a very strong and stable ring complex and act as a molecular bushing for high-speed rotation of the rod acting as a drive shaft. The C-ring, MS-ring, and LP-ring have 34-fold, 34-fold, and 26-fold rotational symmetries, respectively, whereas the rod is a helical assembly consisting of 11 protofilaments. The rod is divided into two structural parts: the proximal rod formed by 6 FliE subunits, 5 FlgB subunits, 6 FlgC subunits, and 5 FlgF subunits in this order; and the distal rod formed by 24 FlgG subunits. The proximal rod is firmly attached to the MS-ring and the polypeptide channel complex formed by 5 FliP subunits, 4 FliQ subunits, and 1 FliR subunit through interactions of FliE with FliF, FliP, and FliR. OM outer membrane, PG peptidoglycan layer, CM cytoplasmic membrane.

Table 1 | CryoEM data collection, processing, refinement, and varidation statistics

	FliF C33 (C1)	FliF C34 (C1)	FliF C11	FliF C33	FliF C34
EMDB PDB	EMD-62211	EMD-62210	EMD-60007 8ZDS	EMD-60008 8ZDT	EMD-60009 8ZDU
Data collection and processing					
Magnification	50,000	50,000	50,000	50,000	50,000
Voltage (kV)	300	300	300	300	300
Electron exposure (e–/Å^2)	40	40	40	40	40
Defocus range (μm)	−0.5 – −2.5	−0.5 – −2.5	−0.5 – −2.5	−0.5 – −2.5	−1.0 – −2.5
Pixel size (Å)	1.00	1.33	1.00	1.00	1.00
Symmetry imposed	C1	C1	C11	C33	C34
Initial particle images (no.)	1,015,741	1,015,741	1,015,741	1,015,741	1,015,741
Final particle images (no.)	70,250	62,306	70,250	70,250	62,306
Map resolution (Å)	4.2	3.6	3.1	2.4	2.5
FSC threshold	0.143	0.143	0.143	0.143	0.143
Refinement					
Initial model used (PDB code)	-	-	7D84, 7CIK	7D84	7D84
Model resolution	-	-	3.70, 2.29	3.70	3.70
FSC threshold	-	-	0.143	0.143	0.143
Model composition					
Non-hydrogen atoms	-	-	69498	40623	42568
Protein residues	-	-	9053	5148	5304
Ligands	-	-	0	0	0
***B* factors (Å^2)**					
Protein	-	-	163.48	38.82	44.73
Ligand	-	-	0	0	0
R.m.s. deviations					
Bond length (Å)	-	-	0.004	0.002	0.001
Bond angles (°)	-	-	0.703	0.444	0.446
Validation					
MolProbity score	-	-	1.73	1.12	1.16
Clash score	-	-	7.65	3.25	3.76
Rotamer outliers (%)	-	-	0.14	0.72	0.00
Ramachandran plot					
Favored (%)	-	-	95.46	99.33	99.33
Allowed (%)	-	-	4.54	0.67	0.67
Disallowed (%)	-	-	0	0	0

the ring structures fell into two distinct classes: 33-mer (70,250 particles, 53% of the population) and 34-mer (62,306 particles, 47% of the population) (Supplementary Fig. 2b). No other symmetries were observed. The MS-ring in the native basal body has 34-fold symmetry[8–10], and C-terminal truncations of FliF result in symmetry variation in the MS-ring[5,10]. The SDS-PAGE band pattern of our purified FliF sample indicates that full-length FliF forms these MS-ring structures (Supplementary Fig. 1a). Because FliF was overexpressed from the plasmid along with FliG and the export-gate proteins, the two rotational symmetries of the MS-ring structure we analyzed in this study might be the result of improper incorporation of the export-gate complex into the MS-ring.

We carried out 3D image reconstruction of the RBM3-ring containing 33 or 34 FliF subunits without imposing rotational symmetry. The resolution was 4.2 Å and 3.6 Å for the 33-mer (EMDB ID: EMD-62211) and 34-mer rings (EMDB ID: EMD-62210), respectively. We then performed iterative 3D refinements with imposed C33 and C34 symmetry, respectively. This process dramatically improved the resolution of the RBM3-ring structure to 2.4 Å and 2.5 Å for the 33-mer (EMDB ID: EMD-60008) and 34-mer (EMDB ID: EMD-60009), respectively (Table 1 and Supplementary Fig. 2). These higher-resolution structures allowed us to construct accurate atomic models of the 33-mer (PDB ID: 8ZDT) and 34-mer (PDB ID: 8ZDU) RBM3-rings (Supplementary Fig. 3). The two atomic models were nearly identical to the previously reported *Salmonella* MS-ring structures (Supplementary Fig. 4), but the map resolutions were better than the previous ones[5–10].

The S-ring domain (residues 230–271 and 381–438) is a globular domain composed of two α-helices (α1 and α2) and an antiparallel three-stranded β-sheet (β1, β6, and β7) (Supplementary Fig. 3b). Residues 397–400 connecting β6 and α2 are invisible. The S-ring domains are horizontally packed with their major axis oriented in the radial direction.

The β-collar domain (residues 272–380) is a long, extended up-and-down β-structure consisting of two sets of antiparallel β-sheets (β2/β5 and β3/β4) (Supplementary Fig. 3b). Intermolecular β2-β5 and β3-β4 interactions create a stable and strong β-barrel structure above the S-ring. In agreement with previous reports[5,8–10], the electron density corresponding to the chain connecting β3 and β4 at the top of the collar (residues 305–354) is very poor, indicating that this chain is highly flexible. The *fliF(N318T)* mutation is located within this flexible region of the β-collar domain and

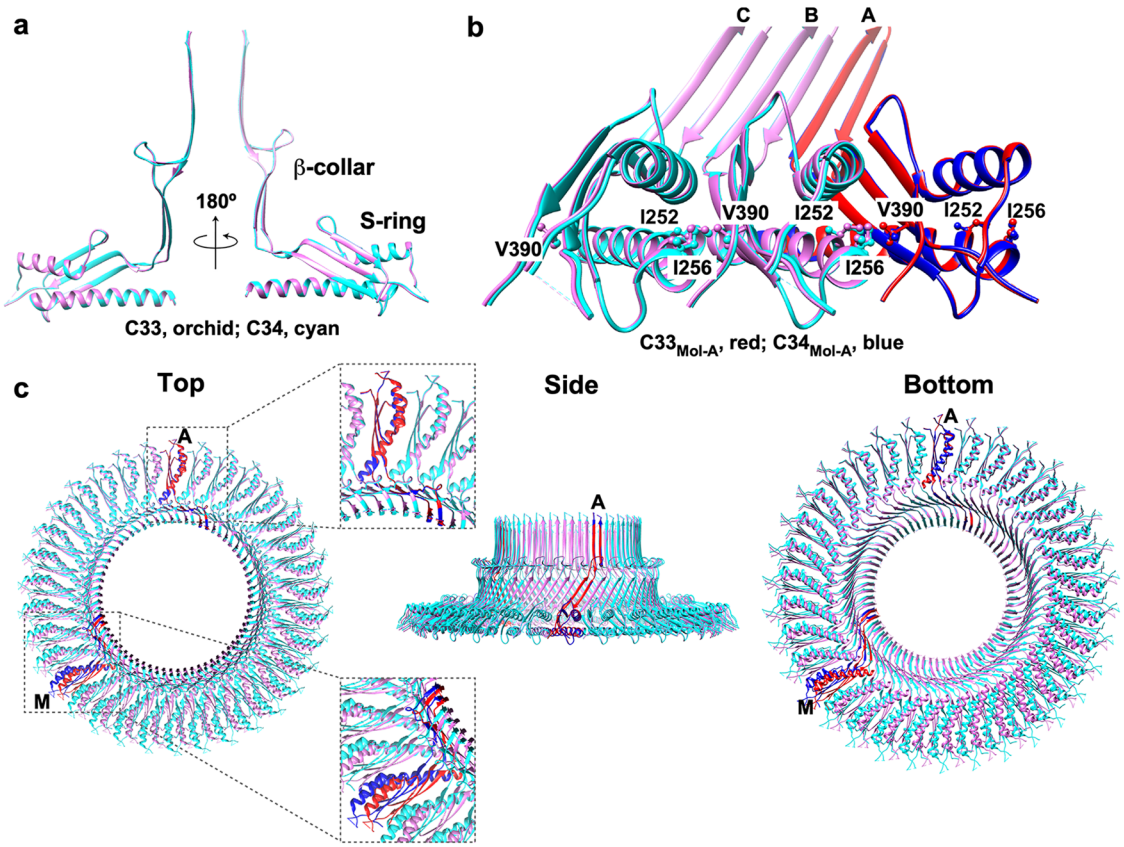

Fig. 2 | Structural comparison of the 33-mer and 34-mer RBM3-rings. a Structural comparison of Mol-A subunits in the 33-mer (PDB ID: 8ZDT) (orchid) and 34-mer (PDB ID: 8ZDU) (cyan) rings. **b** Intermolecular interface between FliF subunits. Only three FliF subunits (Mol-A, Mol-B, Mol-C) are shown. Mol-A (blue) of the 34-mer ring was superimposed on Mol-A (red) of the 33-mer ring. Residues Ile-252, Ile-256, and Val-390 are located at the interface between subunits in the S-ring, and hydrophobic interactions among these three residues contribute to RBM3-ring formation. **c** Superposition of the 33-mer and 34-mer rings.

induces the detachment of the rod-hook-filament structure from the MS-ring under viscous conditions[5,23,36]. Extragenic suppressor mutations in FlgC or FlgF partially suppress such detachment from the MS-ring[36]. These findings suggest that the N318T mutation affects the interaction between the MS-ring and the proximal rod. Because the β-collar acts as a housing for the proximal rod, this flexible region may associate with the rod to prevent it from dislodging from the MS-ring when the flagellar motor operates at high viscous load.

Structural comparison of the 33-mer and 34-mer RBM3-rings

We measured the inner diameters of the 33-mer and 34-mer RBM3-rings (Supplementary Table 2). The inner diameters (derived from least-square fitting of a circle to Cα atoms of Asp-229) of the S-rings were 142 Å for the 33-mer and 146 Å for the 34-mer. The corresponding inner diameters of the β-collars (as derived from least-square fitting of a circle to Cα atoms of Pro-355) were 101 Å and 105 Å (Supplementary Fig. 5). The structures of the S-ring and β-collar domains in the 33-mer and 34-mer rings were nearly identical to each other (Fig. 2a), and the subunit interfaces of the S-ring domains in the 33-mer and 34-mer rings were also almost identical (Fig. 2b).

When a subunit in the 34-mer ring (labeled A in Fig. 2c) was superimposed on a subunit in the 33-mer ring, the offset gradually increased as the subunit position moved away from the superimposed ones, reflecting a slightly different curvature of the two rings (Fig. 2c). When the RBM3 structures of previously reported 33-mer and 34-mer rings were superimposed onto those of our 33-mer and 34-mer rings, subtle differences were observed in the orientation of the S-ring domain relative to the β-collar domain (Supplementary Fig. 4). The result was slight differences in the diameter of the RBM3-ring, even though the rotational symmetry was the same (Supplementary Table 2). Thus, conformational flexibility of the loops connecting the secondary structures within the RBM3 region produces the slight differences in the curvature of the MS-ring and MS-rings with different rotational symmetry[6]. Therefore, we conclude that the small variation in the rotational symmetry of the MS-ring is due to the intrinsic structural flexibility of FliF. This structural flexibility could be an important property to form a fully functional MS-ring efficiently. Because the MS-ring in the native basal body has only C34 symmetry[8–10], we propose that the export-gate complex contributes to the precise determination of the MS-ring curvature.

CryoEM structural analysis of the inner part of the M-ring

To build the atomic model of the inner part of the M-ring formed by the RBM1 and RBM2 domains, we performed iterative 3D refinement of the 33-mer ring with C11 symmetry to obtain a higher-resolution map of the inner core ring formed by 22 RBM2 domains. The improved resolution of the 3D map (EMDB ID: EMD-60007) (Table 1) allowed us to build an atomic model of the inner M-ring. It displayed a structure resembling a gear wheel, with the 22-mer RBM2-ring surrounded by 11 cog-like domains (PDB ID: 8ZDS) (Supplementary Fig. 6). Some blurred densities possibly corresponding to the remaining 22 RBM1 domains were observed around the RBM2-ring, but the image was not clear enough to incorporate them into the atomic model.

FliF showed two distinct conformations in the 33-mer MS-ring. The asymmetric unit of the 33-mer ring, for which the 3D map was reconstructed with C11 symmetry, consists of 3 FliF molecules, Mol-A, Mol-B, and Mol-C. Mol-A and Mol-C contain RBM2 (residues 123–213) and RBM3 (Mol-A, residues 227–438; Mol-C, residues 228–438). Mol-B also contains RBM1 (residues 61–113) (Fig. 3a).

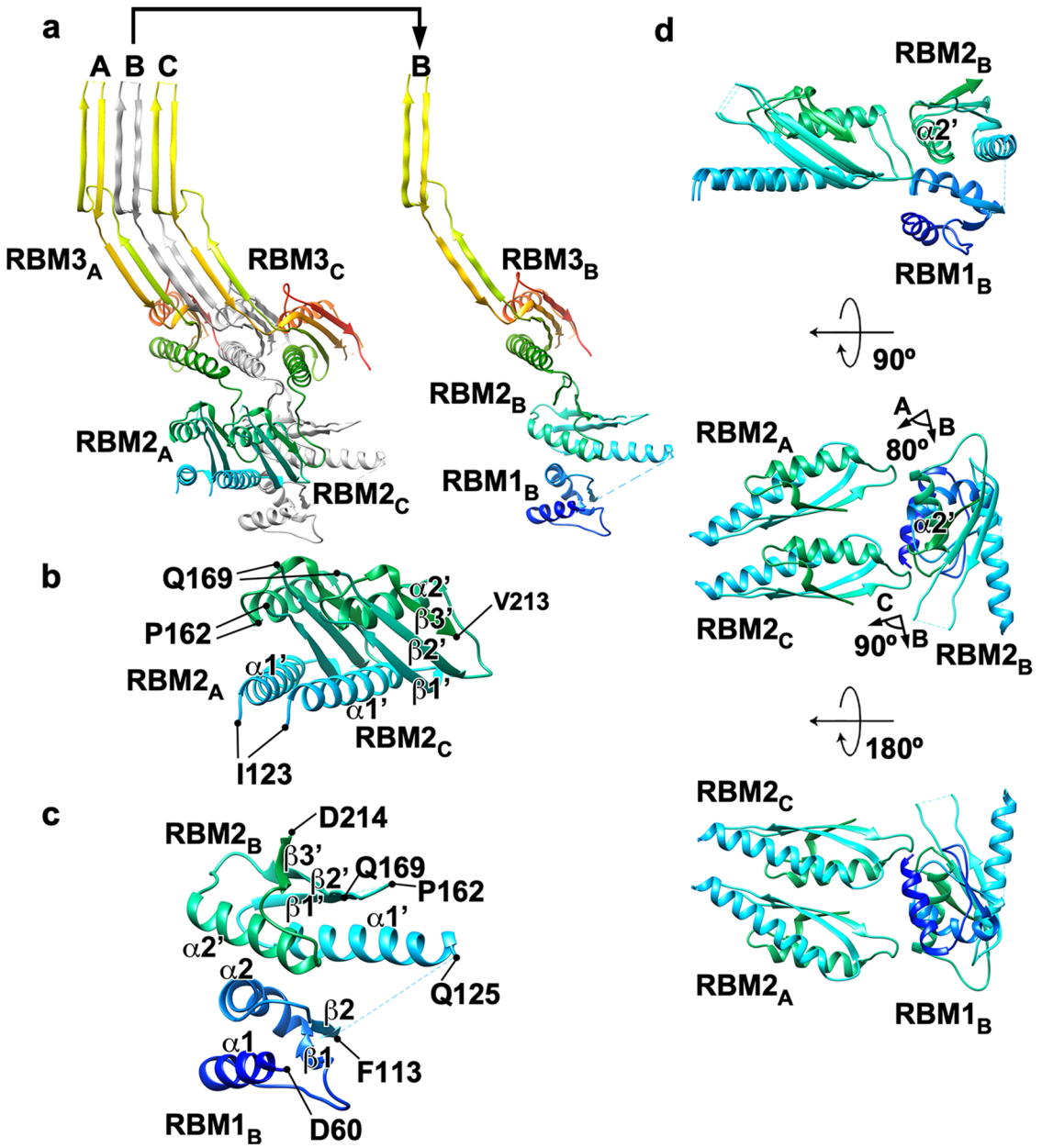

Fig. 3 | The RBM1-RBM2-RBM3-ring structure revealed by C11 symmetry enforcement. a Three FliF subunits (Mol-A, Mol-B, and Mol-C) of an asymmetric unit of the 33-mer ring, viewed from inside the MS-ring. Mol-A and Mol-C consists of RBM2 (residues 123–213) and RBM3 (Mol-A, residues 227–438; Mol-C, residues 228–438) while Mol-B has RBM1 (residues 61–113) in addition to the RBM2 (residues 125–215) and RBM3 (residues 229–438) domains. The RBM2 domains of Mol-A and Mol-C face inward to form the RBM2-ring. The RBM1 and RBM2 domains of Mol-B face outward to form a cog-like structure. **b** Interactions between adjacent RBM2 domains in the RBM2-ring. **c** Interactions between RBM1 and RBM2 in the cog-like structure. **d** Three different views of RBM1-RBM2 of Mol-B in the cog-like structure interacting with 2 RBM2 domains of Mol-A and Mol-C forming the 22-mer RBM2-ring on the left.

RBM1 is composed of two α-helices (α1 and α2) and a parallel two-stranded β-sheet (β1 and β2). RBM2 consists of two α-helices (α1' and α2') and an antiparallel three-stranded β-sheet (β1'–β3'). The density corresponding to residues 163–168 of RBM2 is not resolved well. Although the density corresponding to residues 114–124 connecting RBM1 and RBM2 is poorly resolved in Mol-B, RBM1 associates with RBM2 to stabilize the RBM1-RBM2 structure (RBM1-2) (Fig. 3b, c).

Extensive RBM2-RBM2 intermolecular interactions in Mol-A and Mol-B produce a flat RBM2-ring. The RBM1-2 structure of Mol-B is rotated approximately 90° in the CW direction relative to the RBM2 domain of Mol-A when viewed from outside the ring and approximately 80° in the CCW direction when viewed from above the plane of the ring. It interacts with the two RBM2 domains of Mol-A and Mol-C to create the cog-like structures that are peripheral to the RBM2-ring (Fig. 3d).

Rationale for mutational analyses

Our structural studies indicate that three regions of FliF are good candidates for mutational analysis. One is the i-loop of RBM2 (residues 164–167), which is poorly resolved in our structure but well-defined in the MS-ring of the intact basal body (Fig. 4a). Is it stabilized in the basal body by an interaction with FliP and/or FliR, and is this interaction important in the proper formation and function of the export gate? The second is the loop that connects RBM2 and RBM3 (RBM2-3 loop, residues 214–228) (Fig. 5a). How important is its length and residue composition for generating the two

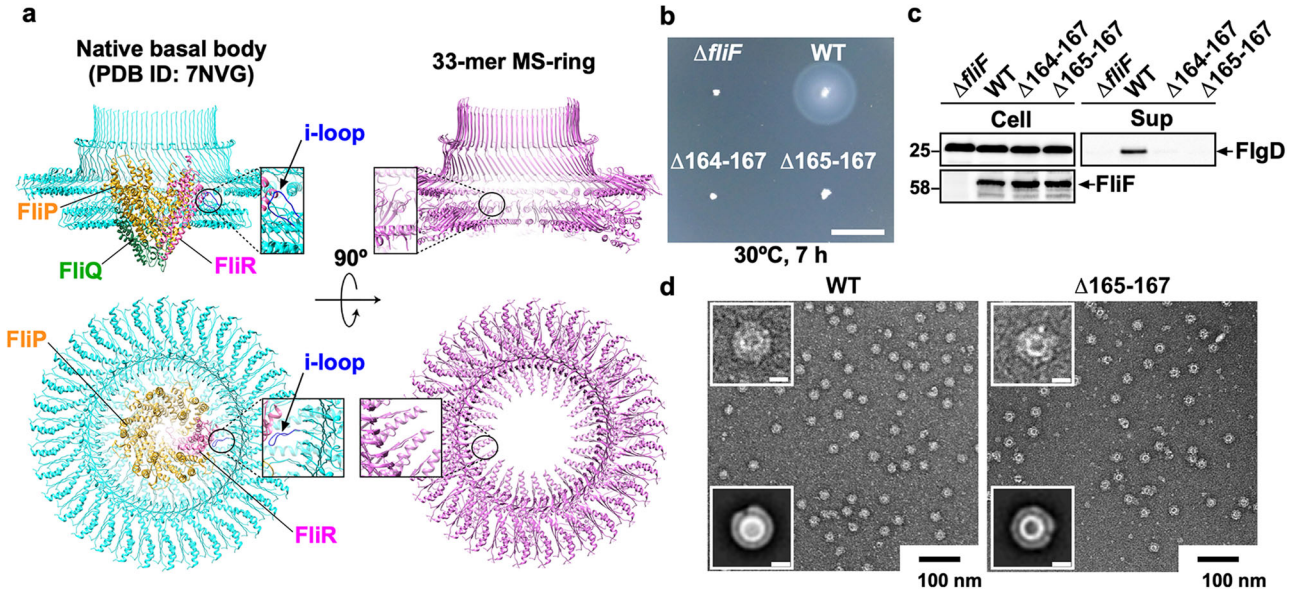

Fig. 4 | Role of the i-loop of FliF in the assembly and function of the MS-ring. **a** Comparison of the i-loop conformations in the native basal body MS-ring (PDB ID: 7NVG) (left) and our 33-mer MS-ring with C11 symmetry applied (PDB ID: 8ZDS) (right). Five FliP subunits (goldenrod) and one FliR subunit (hot pink) assemble into the $FliP_5$-$FliR_1$ complex, and then four FliQ subunit (sea green) surround the $FliP_5$-$FliR_1$ complex. The $FliP_5$-$FliQ_4$-$FliR_1$ complex is formed with a helical array of subunits and is located in the central pore of the RBM2-ring in the native basal body MS-ring. The i-loop of each RBM2 domain (residues 159–172) associates with either FliP or FliR subunit, and hence residues 163–168 are visible (left panels). However, the density corresponding to these residues in the i-loop is poor in our structure. Furthermore, the RBM1 domains below the inner core RBM2-ring are missing in both MS-ring structures. **b** Motility of a *Salmonella fliF* null mutant harboring pTrc99AFF4 (Δ*fliF*), pMKMiF015 (WT), pMKMiF015(Δ164–167) (indicated as Δ164–167), or pMKMiF015(Δ165–167) (indicated as Δ165–167) in soft agar. The plate was incubated at 30 °C for 7 hours. Scale bar, 1.0 cm. At least seven independent measurements were performed. **c** Secretion assays. Whole cell proteins (Cell) and culture supernatant fractions (Sup) were prepared from the above transformants. A 5 µl solution of each protein sample, which was normalized to an optical density of OD_{600}, was subjected to SDS-PAGE, followed by immunoblotting with polyclonal anti-FlgD (first row) or anti-FliF (second row) antibody. The positions of molecular mass markers (kDa) are shown on the left. The regions of interest were cropped from original immunoblots shown in Supplementary Fig. 14. At least three independent assays were performed. **d** Negative stained EM images of the MS-rings isolated from the WT and Δ165–167 cells. Electron micrographs were recorded at a magnification of x50,000. Upper and lower insets indicate enlarged views of the MS-ring and representative 2D class average images calculated by RELION 4.0.0 (See Supplementary 7). Scale bars are shown in insets, 10 nm. Independent sample preparations were carried out at least three times.

different locations of RBM2, one that forms the 22-mer RBM2-ring that encloses the export-gate complex, the other that interacts with RBM1 to form the 11 cogs that surround the RBM2-ring? Finally, hydrophobic contacts between adjacent FliF subunits are presumably important in forming the S-ring (Fig. 2b). Ile-252 in one subunit interacts with Val-390 in the adjacent subunit, and the I252A substitution results in a non-motile phenotype (Fig. 6a)[10]. Can the motility of the *fliF(I252A)* mutant be restored by second mutations that restore a functional MS-ring?

Mutational analysis of the i-loop of RBM2

Each i-loop of the 22 RBM2 domains that form the RBM2-ring makes direct contact with FliP or FliR in the native basal body MS-ring (Fig. 4a)[8,9]. Therefore, we first investigated whether the contact of the i-loop with FliP or FliR is critical for the assembly of the export-gate complex. We constructed two *fliF* deletion mutants lacking either residues 164–167 or residues 165–167 and analyzed their motility in soft agar (Fig. 4b). Immunoblotting with polyclonal anti-FliF antibody revealed that these two deletions did not affect the cellular level of FliF (Fig. 4c). Unlike wild-type FliF, expression of the Δ164–167 and Δ165–167 mutant variants did not restore motility of the Δ*fliF* mutant (Fig. 4b).

To test whether the lack of motility is a consequence of defective protein export, we analyzed the secretion of FlgD, as a representative export substrate of the fT3SS. Immunoblotting with polyclonal anti-FlgD antibody showed that these two deletions inhibited FlgD secretion (Fig. 4c). Because the deletion of residues 165–167 did not inhibit MS-ring formation (Fig. 4d and Supplementary 7), we suggest that direct interaction of each i-loop with FliP or FliR allows the export-gate complex to be efficiently incorporated into the central pore of the RBM2-ring.

The density corresponding to the 23 RBM1 domains that are not bound to RBM2 is poorly resolved, even in the isolated native basal body. Because FlhA and FlhB are missing in the isolated basal body, we propose that RBM1 may be stabilized in the basal body in vivo by binding to these two export-gate proteins.

Mutational analysis of the loop connecting RBM2 and RBM3

The conformation of the RBM2-3 loop (residues 214–228) in Mol-B is very different from those in Mol-A and Mol-C. Thus, FliF adopts two different conformations in the MS-ring (Fig. 5a). Furthermore, conformational flexibility of this loop may allow the position, orientation, and curvature of the RBM2-ring to be adjusted, thereby causing subtle structural differences in this ring (Supplementary Fig. 8). The RBM2-3 loop contains a conserved DQxGxxL motif (residues 214–220), in which the third and fifth residues are commonly hydrophilic (Fig. 5a). To clarify the role of the RBM2-3 loop in the assembly and function of the MS-ring, we constructed two *fliF* deletion mutants lacking either residues 214–220 or residues 221–227 and analyzed their motility in soft agar (Fig. 5b and Supplementary Fig. 9a). Neither deletion affected the cellular level of FliF (Fig. 5c and Supplementary Fig. 9b). Deletion of residues 214–220 resulted in a non-motile phenotype (Fig. 5b), and FlgD was not secreted into the culture media (Fig. 5c). FliF(Δ214-220) formed a ring-like particle, but 2D class averaging revealed that this deletion destabilizes the structure of the entire MS-ring although the β-collar was often seen clearly (Fig. 5d and Supplementary Fig. 10). We suggest that the DQxGxxL motif is required for efficient formation of the RBM2-ring and the cog-like structures outside it. On the other hand, the *fliFΔ(221–227)* mutant displayed a weak motile phenotype (Supplementary Fig. 9a), and

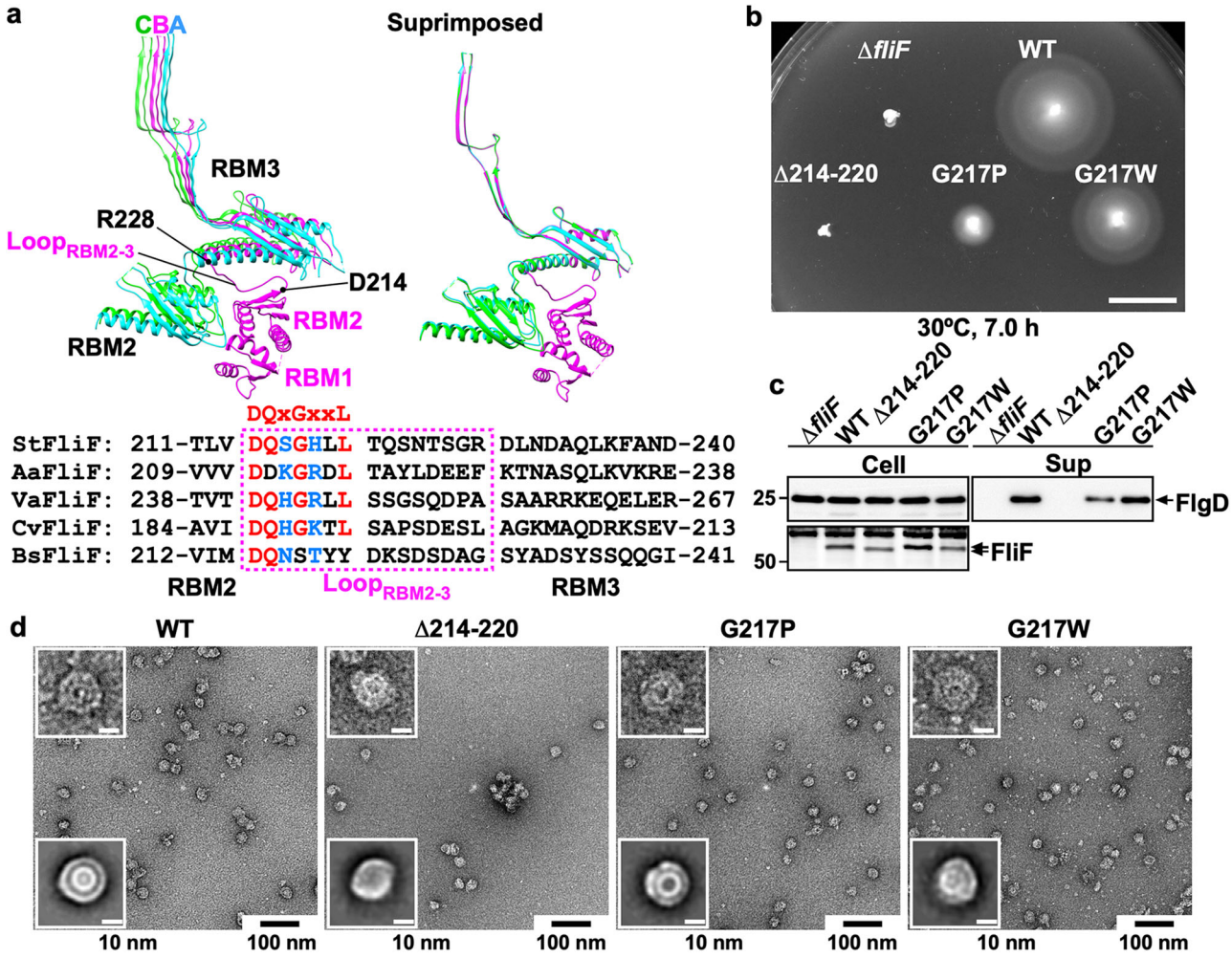

Fig. 5 | Mutational analysis of the RBM2-3 loop. a Structural comparison and multiple sequence alignments of the RBM2-3 loop. Three FliF subunits, Mol-A, Mol-B and Mol-C of the asymmetric unit of the 33-mer MS-ring are shown in the left panel. The RBM2 domains of Mol-A (cyan) and Mol-C (green) form part of the inner core ring, and RBM1-RBM2 of Mol-B (magenta) binds to the outer surface of the RBM2-ring. The three subunits were superimposed with β-collar in the right panel. Multiple sequence alignment was carried out by Clustal Omega. Conserved residues are highlighted in red. The third and fifth residues in the conserved DQxGxxL motif are commonly hydrophilic. UniProt Accession numbers: *Salmonella* (StFliF), P15928; *Aquifex* (AaFliF), A0A7C5L200; marine *Vibrio* (VaFliF), A0A1W6UMQ1; *Caulobacter* (CvFliF), Q04954; *Bacillus* (BsFliF), P23447. **b** Motility of a *Salmonella fliF* null mutant harboring pTrc99AFF4 (indicated as Δ*fliF*), pMKMiF015 (indicated as WT), pMKMiF015(Δ214–220) (indicated as Δ214–220), pMKMiF015(G217P) (indicated as G217P), or pMKMiF015(G217W) (indicated as G217W) in soft agar. The plate was incubated at 30 °C for 7 hours. Scale bar, 1.0 cm. At least seven independent measurements were performed. **c** Flagellar protein secretion assays. Whole cell proteins (Cell) and culture supernatant fractions (Sup) were prepared from the above transformants. A 5 μl solution of each protein sample, which was normalized to an optical density of OD_{600}, was subjected to SDS-PAGE, followed by immunoblotting with polyclonal anti-FlgD (first row) or anti-FliF (second row) antibody. The positions of molecular mass markers (kDa) are shown on the left. The regions of interest were cropped from original immunoblots shown in Supplementary Fig. 15. At least three independent assays were carried out. **d** Negative stained EM images of the MS-rings isolated from the above transformants. Electron micrographs were recorded at a magnification of x50,000. Upper and lower insets indicate enlarged views of the MS-ring and representative 2D class average images calculated by RELION 4.0.0 (See Supplementary Fig. 10). Scale bars shown in insets, 10 nm. Independent sample purification was performed at least three times.

FlgD was secreted, albeit at a lower level than the wild-type (Supplementary Fig. 9b). Since deletion of residues 221–227 did not inhibit MS-ring formation (Supplementary Figs 9c and 10), we suggest that the RBM2-3 loop is also required for efficient incorporation of the export-gate complex into the MS-ring.

To further clarify the role of the DQxGxxL motif in the assembly and function of the MS-ring, we constructed eight *fliF* mutants, *fliF(D214A)*, *fliF(D214E)*, *fliF(D214R)*, *fliF(G217A)*, *fliF(G217P)*, *fliF(G217W)*, *fliF(L219A)*, and *fliF(L220A)*, and analyzed their motility in soft agar (Fig. 5b and Supplementary Fig. 9a). No FliF was seen in the *fliF(D214R)* mutant, whereas FliF was detected at wild-type levels in the remaining mutants (Fig. 5c and Supplementary Fig. 9b). When Arg residues are exposed on the surface of proteins in structurally flexible regions, their C-terminal side is easily cleaved by Arg-C endoprotease. Therefore, the destabilization of FliF by the D214R substitution suggests that the DQxGxxL chain is flexible. The D214A, D214E, L219A, and L220A mutations did not affect motility, indicating that the chemical identity of these three residues is not important (Supplementary Fig. 9a). The G217A and G217W mutations reduced both motility and FlgD secretion slightly, whereas the G217P mutation inhibited both activities (Fig. 5b, c and Supplementary Fig. 9a,b). Because neither the G217A, G217P, nor G217W substitution affected MS-ring formation (Fig. 5d and Supplementary Figs 9c and 10), we suggest that the conformational flexibility of the DQxGxxL motif is important both for efficient formation of the RBM2-ring and cog-like structures and for creation of a central hole of the proper size in the RBM2-ring to accommodate the export-gate complex.

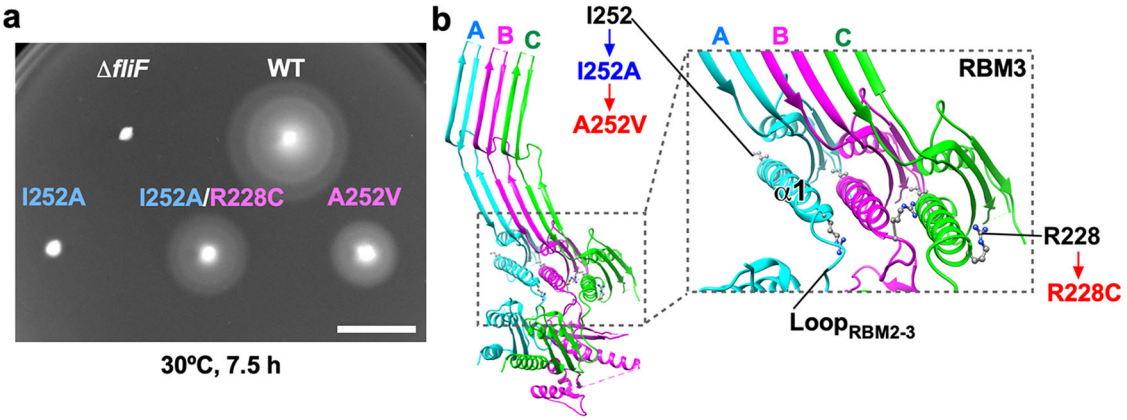

Fig. 6 | Isolation of gain-of-function mutants from the *fliF(I252A)* mutant. **a** Motility of a *Salmonella fliF* null mutant harboring pET3c (indicated as Δ*fliF*), pMKMiF001 (indicated as WT), pMKMiF002 (indicated as I252A), pMKMiF002-SP1 (indicated as I252A/R228C), or pMKMiF002-SP2 (indicated as A252V) in soft agar. The plate was incubated at 30 °C for 7.5 hours. Scale bar, 1.0 cm. At least seven independent measurements were performed. **b** Location of intragenic suppressor mutations isolated from the *fliF(I252A)* mutant. Three FliF subunits (Mol-A, Mol-B, and Mol-C) are viewed from the inside the MS-ring. The I252A mutation and its suppressor mutations are highlighted in blue and red, respectively.

Isolation of up-motile variants from the *fliF(I252A)* mutant

Intermolecular RBM3-RBM3 interactions promote RBM3-ring formation[37]. Ile-252 of RBM3 is located at an interface between adjacent FliF subunits in the MS-ring (Fig. 2b). The *fliF(I252A)* mutation does not affect the formation of the MS-C-ring complex in vivo but significantly reduces the flagellar protein export activity[10]. Thus, this mutation may affect the formation of a central pore of the right size in the RBM2-ring to accommodate the export-gate complex. To test this possibility, we isolated eight up-motile revertants from the *fliF(I252A)* mutant (Fig. 6a). DNA sequencing revealed that one mutation (isolated four times) replaces alanine at position 252 in FliF with valine. The other (also isolated four times) replaces arginine at position 228 in FliF with cysteine (Fig. 6b). The motility of the *fliF(A252V)* mutant was much better than that of the parental mutant although not as good as that of the wild-type strain. Because Ile-252 and Ile-256 make hydrophobic contacts with Val-390 in their neighboring FliF subunit, thereby stabilizing the RBM3-ring (Fig. 2b), the precise length of hydrophobic side chain of residue 252 is important for proper intermolecular RBM3-RBM3 interactions. On the other hand, Arg-228 is located at the N-terminus of the α1-helix of RBM3 in Mol-A and Mol-C and is at the C-terminus of the RBM2-3 loop in Mol-B (Fig. 6b). This result suggests that the I252A substitution affects the orientation of the RBM2-3 loop relative to RBM3. The R228C substitution might induce a conformational change in this loop that compensates for the effect of the I252A replacement, allowing the RBM2-ring to form a central hole of the right size for efficient assembly of the export-gate complex.

Structural modeling of unassembled FliF monomer in the MS-ring

Intermolecular RBM3-RBM3 interactions induce a conformational change in the RBM2-3 loop, allowing 22 RBM2 and 11 RBM1-2 to face inward and outward, respectively. RBM1 regulates proper RBM-2 ring formation[37]. Because the density corresponding to RBM1 is poorly resolved below the RBM2-ring, RBM1 weakly bound to RBM2 in a FliF monomer disengages from RBM2 when RBM2 incorporates into the RBM2-ring. To clarify the mechanism of MS-ring formation, we analyzed intramolecular RBM1-RBM2 and intermolecular RBM2-RBM2 interactions. RBM1 binds to the α1' and α2' helices of RBM2 in the cog-like structure. Leu-98 of RBM1 makes hydrophobic contacts with Leu-147, Ala-193, and Leu-197 of RBM2 (Fig. 7a, left panel). However, these two α-helices of RBM2 are also involved in RBM2-ring formation (Fig. 7a, right panel). Extensive intermolecular interactions between these two α-helices of RBM2 and an antiparallel β-sheet of the neighboring RBM2 as well as intermolecular α1'-α1' interactions promote RBM2-ring formation. In the RBM2-ring, Val-213 of RBM2 of Mol-A makes hydrophobic contacts with Leu-147, Ala-193, and Leu-197 of RBM2 of Mol-C. Furthermore, Phe-126, Gln-133, and Arg-134 of RBM2 of Mol-A interact with Gln-129, Tyr-132, Glu-139 of RBM2 of Mol-C, respectively (Fig. 7a, right panel).

Because the RBM2-3 loop is highly flexible, we fit RBM1-2 onto an RBM2-RBM3 unit in the 33-mer MS-ring and then connected RBM3 with the fitted RBM1-2 at Leu-219 to build a structural model of the monomeric RBM1-RBM2-RBM3 structure (RBM1-3) (Fig. 7b). When two of the RBM1-3 models are placed side by side by fitting their RBM3 domains to those in the 33-mer MS-ring, serious steric hindrance occurs between RBM1 and RBM2 (Fig. 7c, open arrow) or between the RBM1-2 domains of each subunit (Fig. 7d). Because RBM1-2 of one FliF subunit binds to the outside of the ring-forming RBM2 domains of the two closest FliF subunits (Fig. 3d), the RBM1-2 units of the two FliF subunits move during the initial stage of FliF oligomerization. Subsequently, RBM1-2 of one subunit weakly associates with RBM2 of the other. This interaction can be seen in the interaction between Mol-B and Mol-C in the 33-mer MS-ring (Fig. 7e and Supplementary Fig. 11a). Therefore, we propose that this FliF dimer may be an initial complex for MS-ring formation.

Discussion

Although a variation in rotational symmetry has been identified for the MS-ring structures[5,6], only MS-rings with C34 symmetry have been observed in the intact *Salmonella* flagellar basal body[8–10]. FliF folds into two different conformations to form the MS-ring with three different symmetries: C34, C23, and C11. The 34-fold symmetry of the membrane-spanning and cytoplasmic portions of FliF forms the scaffold required for the assembly of FliG, FliM, and FliN into the C-ring[14,15]. The MS-ring also provides a chamber in which the fT3SS export-gate complex assembles. The RBM2-ring assembles with 23-fold symmetry to form a central pore that can stably accommodate the $FliP_5$-$FliQ_4$-$FliR_1$ complex. That complex forms a channel for the export of proteins that form the extracytoplasmic components of the flagellum. It also serves as a structural template for rod assembly[8,9] (Fig. 1). However, the self-assembly mechanism of the MS-ring has been incompletely understood.

To address this question, we performed a high-resolution cryoEM image analysis of the 33-mer MS-ring formed by FliF co-expressed with FliG and the proteins that comprise the export-gate complex. The portion of *Salmonella* FliF containing RBM1, RBM2, and RBM3 forms the RBM2-ring, the S-ring, and the β-collar, suggesting that the two transmembrane helices of FliF are not involved in MS-ring formation. The RBM3 fragment alone can form the S-ring and the β-collar, suggesting that neither RBM1

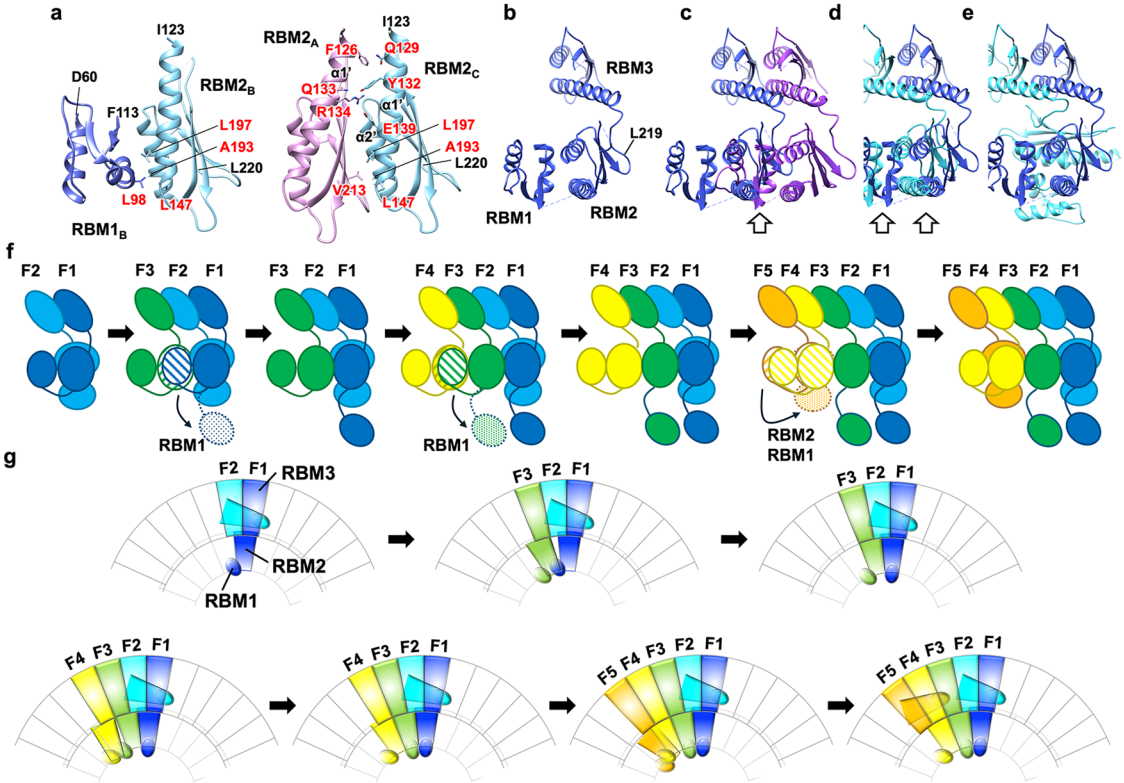

Fig. 7 | Model for MS-ring formation with three different symmetries. a Side-by-side comparison of RBM1-RBM2 in the cog-like structure (left panel) and RBM2-RBM2 forming the RBM2-ring (right panel) shows that both use the same surface of RBM2 for complex formation. The residues involved in the interactions are indicated by labels in red. **b** A plausible structural model of RBM1-RBM2-RBM3 (RBM1-3) as an assembly unit for MS-ring formation. **c** When two RBM1-3 units of Mol-A (violet) and Mol-C (blue) start forming the MS-ring, RBM1 of Mol-A collides with RBM2 of Mol-C (indicated by open arrow). **d** When two RBM1-3 units of Mol-B (cyan) and Mol-C (blue) form a dimer for initiating MS-ring formation, RBM1-2 of Mol-C on the right collides with RBM1-2 of Mol-B on the left (indicated by open arrow). **e** A possible structural model for the initial FliF dimer for MS-ring formation is two RBM1-3 units of Mol-B (cyan) and Mol-C (blue) with RBM1-2 of Mol-B binding to the outer surface of RBM2 of Mol-C forming the inner core ring. The CCW growth model of MS-ring formation viewed from the center (**f**) and periplasmic side (**g**) of the MS-ring. After forming the initial FliF dimer (F1 and F2) (step 1), the third subunit (F3) binds to it, but steric hinderance occurs between RBM2 of F3 and RBM1 of F1 (shown by stripe pattern), thereby inducing the dissociation of RBM1 from RBM2 in F1 and its move to a space below RBM2 (shown by hatched pattern) (step 2). This allows RBM2 of F3 to firmly associate with RBM2 of F1 for initiating inner core ring formation, with RBM1-2 of F2 strongly associated with these two RBM2 units on their outer surface to form a cog-like structure (step 3). The fourth subunit (F4) binds to F3, but steric hinderance between RBM2 of F4 and RBM1 of F3 (shown by stripe pattern) induces the dissociation of RBM1 from RBM2 in F3 and its move to a space below RBM2 of F3 (shown by hatched pattern) (step 4), allowing RBM2 of F4 to firmly associate with RBM2 of F3 (step 5). When the fifth subunit (F5) binds to F4, steric hinderance occurs between two RBM1-2 units of F5 and F4 (shown by stripe pattern) (step 6). To avoid this collision, RBM1-2 of F5 moves outward through a large conformational change of the RBM2-3 loop connecting RBM2 and RBM3 and binds to the outer surface of the RBM2 domains of F3 and F4 to from the second cog-like structure while RBM1 of F4 remains associated with its RBM2 (step 7). The FliF assembly process will proceed by repeating these steps.

nor RBM2 is required for RBM3-ring formation. The RBM2 fragment alone can self-assemble into the RBM2-ring, whereas the RBM1-RBM2 fragment cannot. Because the purified RBM1-RBM2 fragment exits as a stable monomer in solution, this suggests that RBM1 prevents RBM2-ring formation[37]. Therefore, in full-length FliF assembly, intermolecular RBM3-RBM3 interactions first promote the initiation of RBM3-ring formation. This is then followed by the formation of the 22-mer RBM2-ring and 11 cog-like structures just external to the RBM2-ring. Because the RBM1-RBM2 fragment forms a helical tubular structure along with the RBM3 fragment in vitro[36], RBM1 would bind to the oligomerization surface of RBM2 before the next FliF subunit binds, thereby preventing uncontrolled MS-ring formation.

Full-length FliF molecules form the MS-ring with rotational symmetry ranging from 32-fold to 34-fold, with 33-fold being the most common when it is co-expressed with FliG, FliM, and FliN from a plasmid[6]. The symmetry for the 33-mer MS-ring is 33 RBM3 domains (the RBM3-ring), 22 RBM2 domains (the RBM2-ring), and 11 RBM1-2 domains that form the cog-like structures surrounding the RBM2-ring (Supplementary Fig. 6). In the MS-ring in the intact basal body, the observed symmetry is 34 RBM3 domains, 23 RBM2 domains, and 11 RBM1-2 domains. We found that co-expression of FliF with transmembrane export-gate proteins increases the probability of 34-mer MS-ring formation compared to the previous report[6] (Supplementary Fig. 2). Therefore, during the assembly of the MS-ring in vivo, we suggest that constraints imposed by the insertion of the export-gate complex within the RBM2-ring create a space in the RBM3-ring that is filled by a 34th FliF subunit. The resulting structure has 34 RBM3 subunits in the RBM3-ring, 23 RBM2 subunits in the RBM2-ring, 11 RBM1-2 cog-like elements peripheral to the RBM2-ring, and 23 disorganized RBM1 domains beneath the RBM2-ring.

Assuming that a FliF dimer is the initial complex for MS-ring formation (Fig.7b), we propose the following model for MS-ring assembly. The schematic diagrams in Fig. 7f and g are viewed from the center and periplasmic sides of the MS-ring, respectively. After the initial dimer forms (Step 1), RBM3 of the third FliF subunit (F3) binds to RBM3 on the left side of F2. However, because of steric hindrance, RBM1-2 of F3 cannot be placed to the left of RBM2 of F1 (Supplementary Fig. 11b, c). When RBM1-2 of F3 moves closer to RBM1 of F1, they compete with each other for binding to the left surface of RBM2 of F1. Since the intermolecular RBM2-RBM2 interaction is

more extensive than the intramolecular RBM1-RBM2 interaction (Fig. 7a), RBM1-2 of F3 induces the dissociation of RBM1 from RBM2 in F1 (Fig. 7f, g, step 2), and RBM2 of F3 can now associate with RBM2 of F1 to start forming the RBM2-ring (Step 3).

Extensive RBM2-RBM2 interactions not only initiate RBM2-ring formation but also stabilize the first RBM1-2 cog-like structure just outside of the two ring-forming RBM2 domains (Supplementary Fig. 11d). Then, RBM3 of the fourth FliF subunit (F4) binds to the left surface of RBM3 of F3 (Fig. 7f, g, step 4). Again, steric hindrance prevents RBM1-2 of F4 from associating with RBM2 of F3 (Supplementary Fig. 11e) or outside of the two ring-forming RBM2 domains (Supplementary Fig. 11f). Thus, RBM1-2 of F4 replaces RBM1 of F3 (Fig. 7f, g, step 5 and Supplementary Fig. 11g), just as when F3 bound to the initial dimer. Then, RBM3 of the fifth FliF subunit (F5) binds to the left surface of RBM3 of F4 (Fig. 7f, g, step 6). Because of steric hindrance, RBM1-2 of F5 cannot bind to the left of RBM2 of F4. However, because the RBM2 domains of F3 and F4 have already formed a stable docking site, RBM1-2 of F5 can rotate relative to the RBM2 domains of F3 and F4 through a conformational change in the RBM2-3 loop to form the second cog-like unit outside the RBM2-ring (Step 7). By repeating these processes, RBM3-ring assembly proceeds in the CCW direction (viewed from the periplasm), and one RBM1-2 unit out of each three FliF subunits assembled in the ring that is placed outside the RBM2-ring forms the cog-like structure.

Finally, when the 33rd subunit (F33) inserts between F32 and F1, the RBM1 domains of F32 and F33 dissociate from RBM2, thereby not only closing the RBM2-ring with C22 symmetry but also stabilizing the last of the 11 cog-like structures. The 33-mer MS-ring with three different symmetries, C33, C22, and C11, is thus completed (Supplementary Fig. 12a).

The 34-mer MS-ring can be formed through the same process except for the final step. When the 34th subunit (F34) inserts between F33 and F1, the RBM1 domains of F33 and F34 dissociate from RBM2 because of steric hindrance, and extensive interactions of RBM2 of F34 with RBM2 of F1 and F33 close the 34-mer ring with C34, C23 and C11 symmetries (Supplementary Fig. 12b).

In the above model, MS-ring formation proceeds in the CCW direction, but it might also proceed in the CW direction. In the CW growth model for MS-ring formation, RBM3 of F3 binds to RBM3 of F1 in the initial dimer on the right side. Because of steric hindrance, RBM1-2 of F3 cannot be placed on the right side of RBM2 of F1 but can be placed outside the ring-forming RBM2 domains. Unlike the initial dimer formation, RBM1-2 of F3 cannot be stabilized on the outside the ring by binding to RBM2 of other subunits. RBM1-2 of F3 moves freely, and no further growth of FliF assembly would occur (Supplementary Fig. 13). Therefore, we suggest that CCW growth is much more plausible than CW growth.

In summary, we describe how intermolecular domain interactions play a key role in the generation of two conformations of FliF to be assembled into the MS-ring with different interactions between domains. We also propose that a FliF dimer in which each monomer has a different conformation initiates assembly of the MS-ring. The mechanism that we present provides a conceptual advance in understanding how a complex multi-subunit multi-functional protein structure can arise by utilizing different interdomain interactions during its assembly.

Methods

Bacterial strains, plasmids, and DNA manipulations

Bacterial strains and plasmids used in this study are listed in Supplementary Table 2. The pMKM2001 plasmid encodes FliO, His-FliP, HA-FliQ, FliR-FLAG, FlhA, FlhB, FliF, and FliG. FliO, His-FliP, HA-FliQ, FliR-FLAG, FlhA, and FlhB are expressed from a p*trc* promotor whereas FliF and FliG are expressed from an arabinose-inducible promotor. DNA manipulations were performed using standard protocols. Site-directed mutagenesis was carried out using Prime STAR Max Premix as described in the manufacturer's instructions (Takara Bio). All *fliF* mutations were confirmed by DNA sequencing (Eurofins Genomics).

Expression and purification of the MS-ring

A 13 ml of overnight culture of *Salmonella* SJW1368 [Δ(*cheW-flhD*)] cells harboring pMKM20001 (pTrc99CES3/ FliO + His-FliP + HA-FliQ + FliR-FLAG + FlhA + FlhB + FliF + FliG) were inoculated into a 1.3 l of fresh 2×YT [1.6% (w/v) Bacto-tryptone, 1.0% (w/v) Bacto-yeast extract, 0.5% (w/v) NaCl] containing 100 μg ml^{-1} ampicillin, and the cells were grown at 30 °C until the cell density had reached an OD_{600} of about 0.6. After 30 min incubation at 4 °C, arabinose was added at a final concentration of 0.2%, and the cells were grown at 16 °C for 12 hours. The SJW1368 cells co-expressing FliF, FliG, and the transmembrane export gate complex were collected by centrifugation (6400 × *g*, 10 min, 4 °C) and stored at −80 °C. The cells were thawed, resuspended in 80 ml of 50 mM Tris-HCl, pH 8.0, 5 mM EDTA, 50 mM NaCl, and disrupted using a French press at a pressure level of 8000 psi (FA-032, Central Scientific Commerce). After cell debris and undisrupted cells were removed by centrifugation (20,000 × *g*, 20 min, 4 °C), crude membranes were isolated by ultracentrifugation (90,000 × *g*, 1 h, 4 °C). The harvested membranes were solubilized in 44 ml of 50 mM CAPS-NaOH, pH 11.0, 50 mM NaCl, 5 mM EDTA, 1% (w/v) Triton X-100, and left on ice for 1 hour. After centrifugation (20,000 g, 20 min, 4 °C), the supernatant was ultracentrifuged (90,000 × *g*, 1 h, 4 °C), and the pellet was resuspended in 3.8 ml of 25 mM Tris-HCl, pH 8.0, 50 mM NaCl, 1 mM EDTA, 0.1% (w/v) Triton X-100, 0.05% (w/v) lauryl maltose neopentyl glycol (LMNG), and the sample was loaded onto a 15–40% (w/w) sucrose density gradient. After ultracentrifugation (49,100 × *g*, 13 h, 4 °C), fractions containing FlhA, FliF, and FliG were collected (Supplementary Fig. 1) and concentrated by ultracentrifugation (90,000 × *g*, 1 h, 4 °C). The pellet was resuspended in 20 μl of 50 mM Tris-HCl, pH 8.0, 50 mM NaCl, 25 mM imidazole, 0.05% (w/v) Triton X-100, 0.05% (w/v) lauryl maltose neopentyl glycol (LMNG).

Purification and observation of MS-rings by negative staining electron microscopy

A 15 ml solution of the overnight culture of *Salmonella* SJW1368cells transformed with pMKMiF15 (pTrc99AFF4/FliF), pMKMiF15(Δ165–167) [pTrc99AFF4/FliF(Δ165–167)], pMKMiF15(Δ214–220) [pTrc99AFF4/FliF(Δ214–210)], pMKMiF15(Δ221–227) [pTrc99AFF4/FliF(Δ221–227)], pMKMiF15(G217A) [pTrc99AFF4/FliF(G217A)], pMKMiF15(G217P) [pTrc99AFF4/ FliF(G217P)] or pMKMiF15(G217W) [pTrc99AFF4/FliF(G217W)] were inoculated into a 1.5 l of fresh 2×YT medium containing 100 μg ml^{-1} ampicillin and were grown at 30 °C until the cell density had reached an OD_{600} of about 0.6. After 30 min incubation at 4 °C, the cells were grown at 16 °C for 12 hours. The cells were harvested by centrifugation (6400 *g*, 10 min, 4 °C) and stored at −80 °C. The cells were thawed, resuspended in 55 ml of 50 mM Tris-HCl, pH 8.0, 5 mM EDTA, 50 mM NaCl, and disrupted. After centrifugation (20,000 *g*, 15 min, 4 °C) to remove undisrupted cells, cell lysates were ultracentrifuged (90,000 *g*, 1 h, 4 °C). The harvested membranes were suspended in 40 ml of 50 mM CAPS-NaOH, pH 11.0, 50 mM NaCl, 5 mM EDTA, 1% (w/v) Triton X-100 and incubated at 4 °C for 1 hour. After centrifugation (20,000 *g*, 20 min, 4 °C), the supernatants were ultracentrifuged (90,000 g, 60 min, 4 °C), and the pellets were resuspended in 10 mM Tris-HCl, pH 8.0, 5 mM EDTA, 1% Triton-X100 and incubated at 4 °C for 1 hour. The solution was loaded to a 15–40% (w/w) sucrose density gradient in 10 mM Tris-HCl, pH 8.0, 5 mM EDTA, 1% Triton-X100. After ultracentrifugation (49,100 *g*, 13 h, 4 °C), fractions containing FliF were collected and concentrated by ultracentrifugation (90,000 *g*, 60 min, 4 °C). The pellets were resuspended in 30 μl of 25 mM Tris-HCl, pH 8.0, 50 mM NaCl, 1 mM EDTA, 0.05% (w/v) Triton X-100, 0.05% (w/v) LMNG. Sample preparations were performed at least three times.

A 3 μl aliquot of purified MS-ring with or without a certain mutation was placed on a thin carbon-coated copper grid that was glow-discharged for 20 sec. The extra solution was removed from the grid using a paper filter, and the samples were stained with 2% (w/v) uranyl acetate. The grids were dried for at least 30 min at room temperature. Electron micrographs were

taken using JEM-1400Flash (JEOL, Tokyo, Japan) operated at an accelerating voltage of 100 kV and recoded at a magnification of x50,000. To carry out 2D class averaging of the MS-ring structures, particle images were manually picked up, aligned, classified, and averaged using RELION 4.0.0[38].

Sample vitrification and cryoEM data acquisition

Quantifoil Cu 200 mesh R0.6/1.0 holey carbon grids (Quantifoil) were glow discharged on a glass slide for 20 sec. A 2.7 µl aliquot of the sample solution was applied to the grid and blotted by a filter paper for 3 sec at 100% humidity and 4 °C. The grids were quickly frozen in liquid ethane using Vitrobot IV system (Thermo Fisher Scientific). Then, the grids were inserted into a CRYO ARM 300 transmission electron microscopy (JEOL Ltd. Japan) equipped with a cold field-emission electron gun operated at 300 kV and an Ω-type energy filter with a 20 eV slit width. CryoEM images were recorded with a K3 direct electron detector camera (Gatan, USA) at a nominal magnification of ×50,000, corresponding to an image pixel size of 1.0 Å, using SerialEM[39]. The holes were detected using YoneoLocr[40]. Movie frames were recorded in CDS counting mode with a total exposure time of 3 sec and a total dose of ~40 electrons $Å^{-2}$. Each movie was fractionated into 40 frames. In total, 4885 movies were collected.

Image processing of the MS-ring

Single particle analyses of the MS-ring were performed using RELION 3.1[38]. Image processing procedures of the MS-ring are described in Supplementary Fig. 2. After performing motion corrections to align all micrographs, followed by the estimation of parameters of the contrast transfer fraction (CTF), particle images were automatically selected via LoG auto-picking, and the selected particles were extracted into a box of 512 × 512 pixels (1,015,741 particles). Particle images from good 2D class average images were selected for the initial 3D model. In total, 757,555 particles were subjected to 3D classification with C1 symmetry into five classes. A 3D class with good MS ring geometry was further divided into three classes with C1 symmetry; two more iterations of the 3D classification resulted in two different good 3D classes. One had C33 symmetry, and the other had C34 symmetry. After 3D refinement for each of these two classes, post-processing yielded the 3D maps of the 33-mer and 34-mer rings with resolutions of 4.2 Å (216,718 particles) and 3.6 Å (194,233 particles), respectively, according to 0.143 criterion of the Fourier shell correlation (FSC). Then the C33 or C34 symmetry was applied for further image analysis to obtain much the 3D maps with much higher resolutions. After three rounds of CTF refinement and polish, the 3D maps of the 33-mer and 34-mer RBM3-rings were obtained at 2.4 Å and 2.5 Å resolutions, respectively. To obtained detailed structural information on the inner and middle parts of the M-ring, C11 symmetry was applied to the 33-mer ring structure after several iterations of the 3D classification from particles with C33 symmetry. The map of the MS ring with C11 symmetry was obtained at 3.1 Å resolution (68,598 particles). The cryoEM density maps were deposited into Electron Microscopy Data Bank with accession codes EMD-62211 for the 33-mer MS-ring for C1 symmetry imposed, EMD-60007 for the 33-mer MS-ring with C11 symmetry applied, EMD-60008 for the 33-mer RBM3-ring with C33 symmetry applied, EMD-62210 for the 34-mer MS-ring with C1 symmetry applied, and EMD-60009 for the 34-mer RBM3-ring with C34 symmetry applied.

Model building and refinement of the MS-ring structure

The atomic models of the RBM3-ring with C33 or C34 symmetry and the MS-ring with C11 symmetry were constructed using Coot[41]. PHENIX was used for real-space refinement based on the cryoEM maps[42]. The refinement statistics are summarized in Table 1. The atomic coordinates of the FliF complex have been deposited in the Protein Data Bank with accession codes 8ZDS for MS-ring with C11 symmetry applied, 8ZDT for RBM3-ring with C33 symmetry applied, 8ZDU for RBM3-ring with C34 symmetry applied.

Motility assays in soft agar

Fresh transformants were inoculated into soft agar plates [1.0% (w/v) Bacto-tryptone, 0.5% (w/v) NaCl, 0.35% (w/v) agar] containing 100 µg/ml ampicillin and incubated at 30 °C. The assay was performed at least seven times to confirm the reproducibility of the results.

Secretion assay

A 100 µl of the overnight culture of *Salmonella* cells was inoculated into a 5 ml of fresh L-broth [1% (w/v) Bacto-tryptone, 0.5% (w/v) Bacto-yeast extract, 0.5% (w/v) NaCl] containing 100 µg/ml ampicillin and incubated at 30 °C with shaking until the cell density had reached an OD_{600} of ca. 1.4–1.6. Cultures were centrifuged to obtain cell pellets and culture supernatants, separately. The cell pellets were resuspended in sodium dodecyl sulfate (SDS)-loading buffer solution [62.5 mM Tris-HCl, pH 6.8, 2% (w/v) SDS, 10% (w/v) glycerol, 0.001% (w/v) bromophenol blue] containing 1 µl of 2-mercaptoethanol. Proteins in each culture supernatant were precipitated by 10% trichloroacetic acid and suspended in a Tris/SDS loading buffer (one volume of 1 M Tris, nine volumes of 1 X SDS-loading buffer solution) containing 1 µl of 2-mercaptoethanol. Both whole cellular proteins and culture supernatants were normalized to the cell density of each culture to give a constant cell number. After sodium dodecyl sulfate-polyacrylamide gel electrophoresis (SDS-PAGE), immunoblotting with polyclonal anti-FlgD or anti-FliF antibody as the primary antibody and anti-rabbit IgG, HRP-linked whole Ab Donkey (GE Healthcare) as the secondary antibody was carried out using iBind Flex Western Device as described in the manufacturer's instructions (Thermo Fisher Scientific). Detection was performed with Amersham ECL Prime western blotting detection reagent (Cytiva). Chemiluminescence signals were captured by a Luminoimage analyzer LAS-3000 (GE Healthcare). Bands of prestained protein molecular weight markers (Bio-Rad) transferred to each membrane were also photographed with the LAS-3000 under brightfield illumination and combined with each immunoblot image to identify the band of interest. All image data were processed with Photoshop (Adobe). At least three independent experiments were performed.

Multiple sequence alignment

Multiple sequence alignment was performed by Clustal Omega (https://www.ebi.ac.uk/jdispatcher/msa/clustalo).

Statistics and reproducibility

The cryoEM data collection, processing, and refinement statistics are summarized in Table 1. Sample sizes and the number of replicates are described in the corresponding methods and figure legends.

Data availability

The cryoEM maps have been deposited in the Electron Microscopy Data Bank under accession codes EMD-60007 for the 33-mer MS-ring with C11 symmetry applied, EMD-60008 for the 33-mer MS-ring with C33 symmetry applied, EMD-60009 for the 34-mer MS-ring with C34 symmetry applied, EMD-62210 for the 34-mer MS-ring with C1 symmetry imposed, and EMD-62211 for the 33-mer MS-ring with C1 symmetry imposed. The atomic coordinates for the MS-ring with C11, C33, and C34 symmetry applied have deposited in the Protein Data Bank under accession codes 8ZDS, 8ZDT, 8ZDU, respectively. All data generated during this study are included in this published article and its Supplementary Information. Strains, plasmids, polyclonal antibodies, and all other data are available from the corresponding author upon request.

Received: 20 August 2024; Accepted: 7 January 2025;
Published online: 16 January 2025

References

1. Nakamura, S. & Minamino, T. Flagella-driven motility of bacteria. *Biomolecules* **9**, 279 (2019).

2. Minamino, T. & Kinoshita, M. Structure, assembly, and function of flagella responsible for bacterial locomotion. *EcoSal Plus* eesp-0011-eesp-2023 (2023).
3. Minamino, T. & Imada, K. The bacterial flagellar motor and its structural diversity. *Trends Microbiol.* **23**, 267–274 (2015).
4. Terashima, H., Kawamoto, A., Morimoto, Y. V., Imada, K. & Minamino, T. Structural differences in the bacterial flagellar motor among bacterial species. *Biophys. Physicobiol.* **14**, 191–198 (2017).
5. Johnson, S. et al. Symmetry mismatch in the MS-ring of the bacterial flagellar rotor explains the structural coordination of secretion and rotation. *Nat. Microbiol.* **5**, 966–975 (2020).
6. Singh, P. K., Cecchini, G., Nakagawa, T. & Iverson, T. M. CryoEM structure of a post-assembly MS-ring reveals plasticity in stoichiometry and conformation. *PLoS One* **18**, e0285343 (2023).
7. Takekawa, N. et al. Structural analysis of S-ring composed of FliFG fusion proteins in marine *Vibrio* polar flagellar motor. *mBio* **15**, e01261-24 (2024).
8. Johnson, S. et al. Molecular structure of the intact bacterial flagellar basal body. *Nat. Microbiol.* **6**, 712–721 (2021).
9. Tan, J. et al. Structural basis of assembly and torque transmission of the bacterial flagellar motor. *Cell* **184**, 2665–2679.e19 (2021).
10. Kawamoto, A. et al. Native flagellar MS ring is formed by 34 subunits with 23-fold and 11-fold subsymmetries. *Nat. Commun.* **12**, 4223 (2021).
11. Ueno, T., Oosawa, K. & Aizawa, S. M ring, S ring and proximal rod of the flagellar basal body of *Salmonella typhimurium* are composed of subunits of a single protein, FliF. *J. Mol. Biol.* **227**, 672–6777 (1992).
12. Ueno, T., Oosawa, K. & Aizawa, S. Domain structures of the MS ring component protein (FliF) of the flagellar basal body of *Salmonella typhimurium*. *J. Mol. Biol.* **236**, 546–555 (1994).
13. Francis, N. R., Irikura, V. M., Yamaguchi, S., DeRosier, D. J. & Macnab, R. M. Localization of the *Salmonella typhimurium* flagellar switch protein FliG to the cytoplasmic M-ring face of the basal body. *Proc. Natl Acad. Sci. USA* **89**, 6304–6308 (1992).
14. Johnson, S. et al. Structural basis of directional switching by the bacterial flagellum. *Nat. Microbiol.* **9**, 1282–1292 (2024).
15. Singh, P. K. et al. CryoEM structures reveal how bacterial flagellum rotates and switches direction. *Nat. Microbiol.* **9**, 1271–1281 (2024).
16. Thomas, D. R., Morgan, D. G. & DeRosier, D. J. Rotational symmetry of the C ring and a mechanism for the flagellar rotary motor. *Proc. Natl Acad. Sci. USA* **96**, 10134–10139 (1999).
17. Thomas, D. R., Francis, N. R., Xu, C. & DeRosier, D. J. The three-dimensional structure of the flagellar rotor from a clockwise-locked mutant of *Salmonella enterica* serovar typhimurium. *J. Bacteriol.* **188**, 7039–7048 (2006).
18. Sakai, T. et al. Novel insights into conformational rearrangements of the bacterial flagellar switch complex. *mBio* **10**, e00079-19 (2019).
19. Nakamura, S. & Minamino, T. Structure and dynamics of the bacterial flagellar motor complex. *Biomolecules* **14**, 1488 (2024).
20. Minamino, T., Kinoshita, M. & Namba, K. Directional switching mechanism of the bacterial flagellar motor. *Comput. Struct. Biotechnol. J.* **17**, 1075–1081 (2019).
21. Yamaguchi, T. et al. Structure of the molecular bushing of the bacterial flagellar motor. *Nat. Commun.* **12**, 4469 (2021).
22. Fujii, T. et al. Identical folds used for distinct mechanical functions of the bacterial flagellar rod and hook. *Nat. Commun.* **8**, 14276 (2017).
23. Okino, H. et al. Release of flagellar filament-hook-rod complex by a *Salmonella typhimurium* mutant defective in the M ring of the basal body. *J. Bacteriol.* **171**, 2075–2082 (1989).
24. Minamino, T., Yamaguchi, S. & Macnab, R. M. Interaction between FliE and FlgB, a proximal rod component of the flagellar basal body of *Salmonella*. *J. Bacteriol.* **182**, 3029–3036 (2000).
25. Minamino, T., Imada, K. & Namba, K. Mechanisms of type III protein export for bacterial flagellar assembly. *Mol. BioSyst.* **4**, 1105–1115 (2008).
26. Minamino, T., Kinoshita, M. & Namba, K. Insight into distinct functional roles of the flagellar ATPase complex for flagellar assembly in *Salmonella*. *Front. Microbiol.* **13**, 864178 (2022).
27. Minamino, T., Kinoshita, M., Morimoto, Y. V. & Namba, K. Activation mechanism of the bacterial flagellar dual-fuel protein export engine. *Biophys. Physicobiol.* **19**, e190046 (2022).
28. Lynch, M. J. et al. Co-Folding of a FliF-FliG split domain forms the basis of the MS:C ring interface within the bacterial flagellar motor. *Structure* **25**, 317–328 (2017).
29. Takekawa, N. et al. Two distinct conformations in 34 FliF subunits generate three different symmetries within the flagellar MS-ring. *mBio* **12**, e03199-20 (2021).
30. Fukumura, T. et al. Assembly and stoichiometry of the core structure of the bacterial flagellar type III export gate complex. *PLoS Biol.* **15**, e2002281 (2017).
31. Fabiani, F. D. et al. A flagellum-specific chaperone facilitates assembly of the core type III export apparatus of the bacterial flagellum. *PLoS Biol.* **15**, e2002267 (2017).
32. Kihara, M., Minamino, T., Yamaguchi, S. & Macnab, R. M. Intergenic suppression between the flagellar MS ring protein FliF of *Salmonella* and FlhA, a membrane component of its export apparatus. *J. Bacteriol.* **183**, 1655–1662 (2001).
33. Morimoto, Y. V. et al. Assembly and stoichiometry of FliF and FlhA in *Salmonella* flagellar basal body. *Mol. Microbiol.* **91**, 1214–1226 (2014).
34. Abrusci, P. et al. Architecture of the major component of the type III secretion system export apparatus. *Nat. Struct. Mol. Biol.* **20**, 99–104 (2013).
35. Kawamoto, A. et al. Common and distinct structural features of *Salmonella* injectisome and flagellar basal body. *Sci. Rep.* **3**, 3369 (2013).
36. Komatsu, H. et al. Genetic analysis of revertants isolated from the rod-fragile *fliF* mutant of *Salmonella*. *Biophys. Physicobiol.* **13**, 13–25 (2016).
37. Mariano, G. et al. Oligomerization of the FliF domains suggests a coordinated assembly of the bacterial flagellum MS ring. *Front. Microbiol.* **12**, 781960 (2022).
38. Scheres, S. H. W. RELION: Implementation of a Bayesian approach to cryo-EM structure determination. *J. Struct. Biol.* **180**, 519–530 (2012).
39. Mastronarde, D. N. Automated electron microscope tomography using robust prediction of specimen movements. *J. Struct. Biol.* **152**, 36–51 (2005).
40. Yonekura, K., Maki-Yonekura, S., Naitow, H., Hamaguchi, T. & Takaba, K. Machine learning-based real-time object locator/evaluator for cryo-EM data collection. *Commun. Biol.* **4**, 1044 (2021).
41. Emsley, P., Lohkamp, B., Scott, W. G. & Cowtan, K. Features and development of *Coot*. *Acta Crystallogr. D. Struct. Biol.* **66**, 486–501 (2010).
42. Liebschner, D. et al. Macromolecular structure determination using X-rays, neutrons and electrons: recent developments in Phenix. *Acta Crystallogr. D. Struct. Biol.* **75**, 861–877 (2019).

Acknowledgements

We thank Kelly T. Hughes for his kind gift of a *Salmonella fliF* null mutant and Yasuyo Abe and Yoshie Kushima for technical assistance. This work was supported in part by JSPS KAKENHI Grant Numbers JP20K15749 and JP22K06162 (to M.K.) and JP19H03182, JP22H02573, and JP22K19274 (to T.Minamino) and MEXT KAKENHI Grant Numbers JP20H05532, and JP22H04844 (to T.Minamino). This work has also been supported by Platform Project for Supporting Drug Discovery and Life Science Research (BINDS) from AMED under Grant Number JP19am0101117 and JP21am0101117 (to K.N.), by the Cyclic Innovation for Clinical Empowerment (CiCLE) from AMED under Grant Number JP17pc0101020 (to K.N.), and by JEOL YOKOGUSHI Research Alliance Laboratories of Osaka University (to K.N.).

Author contributions

T.Minamino and K.N. conceived and designed research; M.K. prepared samples for cyroEM; M.K., F.M., and T.Miyata collected and analysed cryoEM image data; M.K. and K.I. built atomic models; M.K. and T.Minamino performed genetic, biochemical, and physiological experiments; T.Minamino, K.I., and K.N. wrote the paper based on discussion with other authors.

Competing interests

The authors declare no competing interests.

Additional information

Supplementary information The online version contains supplementary material available at https://doi.org/10.1038/s42003-025-07485-2.

Correspondence and requests for materials should be addressed to Keiichi Namba or Tohru Minamino.

Peer review information *Communications Biology* thanks Michael D Manson and the other, anonymous, reviewer(s) for their contribution to the peer review of this work. Primary Handling Editors: Janesh Kumar and Laura Rodríguez Pérez.